Rock Mech Rock Eng (2014) 47:187–206
DOI 10.1007/s00603-012-0354-7

ORIGINAL PAPER

Numerical Modelling of the Anisotropic Mechanical Behaviour of Opalinus Clay at the Laboratory-Scale Using FEM/DEM

Andrea Lisjak · Bryan S. A. Tatone · Giovanni Grasselli · Tim Vietor

Received: 5 December 2012 / Accepted: 8 December 2012 / Published online: 27 December 2012

Abstract The Opalinus Clay (OPA) is an argillaceous rock formation selected to host a deep geologic repository for high-level nuclear waste in Switzerland. It has been shown that the excavation damaged zone (EDZ) in this formation is heavily affected by the anisotropic mechanical response of the material related to the presence of bedding planes. In this context, the purpose of this study is twofold: (i) to illustrate the new developments that have been introduced into the combined finite-discrete element method (FEM/DEM) to model layered materials and (ii) to demonstrate the effectiveness of this new modelling approach in simulating the short-term mechanical response of OPA at the laboratory-scale. A transversely isotropic elastic constitutive law is implemented to account for the anisotropic elastic modulus, while a procedure to incorporate a distribution of preferentially oriented defects is devised to capture the anisotropic strength. Laboratory results of indirect tensile tests and uniaxial compression tests are used to calibrate the numerical model. Emergent strength and deformation properties, together with the simulated damage mechanisms, are shown to be in strong agreement with experimental observations. Subsequently, the calibrated model is validated by investigating the effect of confinement and the influence of the loading angle with respect to the specimen anisotropy. Simulated fracture patterns are discussed in the context of the theory of brittle rock failure and analyzed with reference to the EDZ formation mechanisms observed at the Mont Terri Underground Research Laboratory.

Keywords Opalinus Clay · Rock anisotropy · FEM/DEM · Brittle failure

A. Lisjak (✉) · B. S. A. Tatone · G. Grasselli
Department of Civil Engineering, University of Toronto, Toronto, Canada
e-mail: andrea.lisjak@utoronto.ca

B. S. A. Tatone
e-mail: bryan.tatone@utoronto.ca

G. Grasselli
e-mail: giovanni.grasselli@utoronto.ca

T. Vietor
National Cooperative for the Disposal of Radioactive Waste (NAGRA), Wettingen, Switzerland
e-mail: tim.vietor@nagra.ch

1 Introduction

Opalinus clay (OPA) is indurated over-consolidated clay shale that has been chosen as a host rock formation for a high-level nuclear waste underground repository in Switzerland. The key characteristics that make this argillaceous rock suitable for radioactive waste storage include: low permeability, low diffusion coefficients and good retention capacity for radionuclides, self-sealing properties, and lack of economic value. Nevertheless, one of the main concerns is that these favourable long-term isolation properties could be negatively affected by the disturbance and damage associated with the underground excavations comprising the repository. The micro-cracked zone surrounding such openings, characterized by damage and permeability increased by several orders of magnitude is termed the excavation damaged zone (EDZ) (Tsang et al. 2005). To determine the shape and extent of the EDZ, a correct understanding and prediction of the mechanical behaviour of OPA is of paramount importance.

Opalinus clay is characterized by a preferably oriented micro-structure which results in a distinct anisotropy of its hydro-mechanical properties. This material anisotropy has

been largely documented by several laboratory testing campaigns on specimens from the Mont Terri Underground Research Laboratory (URL) (e.g., Naumann et al. 2007; Popp and Salzer 2007a; Bock 2009; Jahns 2010). Other recent laboratory results clearly show that the failure process in OPA, including the stress–strain response, fracture mechanisms and acoustic activity, is typical of that for brittle materials (Amann et al. 2011, 2012).

Laboratory evidence regarding the key-role played by the material anisotropy in controlling the brittle failure of OPA is confirmed by in situ observations at the Mont Terri URL. Macroscopic excavation-parallel extensional fractures have been reported in the near-field of numerous test tunnels and a distinctive variation of failure mechanism has been observed as a function of the orientation of the tunnel with respect to the bedding plane orientation (Bossart et al. 2002; Blümling et al. 2007). Furthermore, the influence of strength anisotropy on borehole damaged zones has recently been demonstrated by the fracture patterns observed in over-cored resin-injected boreholes (Vietor et al. 2012) and in-hole camera recording (Seeska and Lux 2012).

The current work is motivated by the need to develop and validate numerical tools that could assist in the design of deep geological repositories. In particular, numerical tools that are capable of reproducing the observed rock mass failure mechanisms, including the shape and extent of the EDZ, are required. Considering the failure process of OPA, the employed numerical model must be able to simulate the intrinsic anisotropy of the material and the localization of failure.

In this paper, new developments that allow geomaterials, with anisotropic deformation and strength characteristics, to be modelled using the combined finite-discrete element method (FEM/DEM) are presented (Sect. 3). The effectiveness of the numerical approach is then demonstrated by quantitatively reproducing the short-term response of OPA observed during standard rock mechanics tests. In particular, calibration of the model, based upon unconfined compression and indirect tension test results, is discussed (Sect. 4). In Sect. 5, the model is validated by simulating the effect of confinement and the orientation of specimen anisotropy on the mechanical behaviour of OPA. Modelling results are compared to published laboratory findings for OPA and other anisotropic rocks and are discussed in the context of the EDZ formation mechanisms observed at the Mont Terri URL. Finally, the mesh sensitivity of the proposed FEM/DEM model and its applicability to large-scale problems are discussed (Sect. 6).

2 Modelling Progressive Failure Processes of Anisotropic Rocks

The approaches available in computational geomechanics to model the damage process of anisotropic rock materials are generally classified as: (i) the equivalent continuum approach, (ii) the discrete element method (DEM) and (iii) the hybrid approach.

With the continuum method, the presence of layers is smeared to produce a fictitious continuous material that exhibits mechanical characteristics that are similar to the original discontinuous medium. That is, the effect of layering is implicit in the choice of the material stress–strain constitutive laws. Traditional formulations of the equivalent continuum approach for anisotropic rocks are the Ubiquitous Joint Model, implemented for example in the commercial code FLAC (Itasca Consulting Group Inc. 2012) and models based on the Cosserat theory (e.g., Adhikary and Dyskin 1998; Riahi and Curran 2009). Localization of failure in classic continuum elasto-plastic formulations is captured by either enriching the continuum with micro-structural effects such as the second gradient damage models (e.g., Besuelle et al. 2006; Collin et al. 2006) or using statistical damage models (e.g., Jia and Tang 2008).

With the DEM approach, layers or joints are explicitly represented in the numerical model. The medium is modeled as an assembly of rigid or deformable particles or blocks with interaction laws governing the emergent behaviour of the material. Examples of anisotropic rock modelling using particle-based DEM codes are given by Potyondy and Cundall (2000), Konietzky et al. (2003), Potyondy and Cundall (2004), and You et al. (2011). Although the large computational demand tends to limit its applicability to small-scale problems, the DEM approach offers unique advantages when the extended loss of continuity inside the material, for example due to the progressive breakdown, makes continuum constitutive models inappropriate.

The third category, hybrid continuum/discontinuum approaches (e.g., Dedecker et al. 2007), combines DEM techniques to represent zones affected by strong non-linear behaviour due to material failure with a continuum approach for the remaining small-strain elastic regions. The hybrid method known as the combined finite-discrete element method (FEM/DEM) (Munjiza 2004), represents a particular type of hybrid approach whereby the elastic deformation of the material is described using continuum mechanics theory while DEM algorithms and non-linear fracture mechanics principles are employed to capture fracture mechanisms that are typical of brittle and quasi-brittle materials such as concrete and rocks.

3 Fundamental Principles of the FEM/DEM Approach

The combined finite/discrete element method (FEM/DEM) is a numerical method pioneered by Munjiza et al. (1995)

for the dynamic simulation of multiple interacting deformable bodies. A unique feature of such a numerical tool is the ability to model the transition from continuum to discontinuum by explicitly simulating fracture and fragmentation processes. In the following sub-sections, the key processes of the method are described with particular emphasis on the approach that was developed to capture the behaviour of anisotropic rocks, including OPA. The anisotropy modelling capability was implemented into the two-dimensional Y-Geo FEM/DEM code (Mahabadi et al. 2012a), which represents an extension of the original Y2D code of Munjiza (2004) undergoing development at the University of Toronto for geomechanical applications.

3.1 Interaction of Discrete Bodies

A FEM/DEM simulation can comprise a very large number of potentially interacting distinct elements. To correctly capture this behaviour, contacting couples (i.e., pairs of contacting discrete elements) must first be detected. Subsequently, the interaction forces resulting from such contacts can be defined. Contact interaction forces are calculated between all pairs of elements that overlap in space. Two types of forces are applied to the elements of each contacting pair: repulsive forces and frictional forces.

The repulsive forces between the elements of each contacting pair (i.e., couples) are calculated using a penalty function method (Munjiza and Andrews 2000). Contacting couples tend to penetrate into each other, generating distributed contact forces, which depend on the shape and size of the overlap between the two bodies and the value of the penalty term. As penalty values tend to infinity, a body impenetrability condition is approached.

The frictional forces between contacting couples are calculated using a Coulomb-type friction law. These frictional forces are used to simulate the shear strength of intact material and of pre-existing and newly created fractures.

3.2 Material Failure

Damage and failure of rock material is simulated in FEM/DEM by explicitly modelling crack initiation and propagation using principles of non-linear elastic fracture mechanics (NLEFM). According to this theory, originally developed for metals by Dugdale (1960) and Barenblatt (1962), when the ultimate strength of the material is reached, a zone characterized by non-linear behaviour starts to form ahead of the crack tip. This zone is known as the fracture process zone (FPZ). In rocks, the FPZ is characterized by interlocking and micro-cracking (Labuz et al. 1985) (Fig. 1a). The material in the FPZ, albeit damaged, is still able to transfer load across the crack walls (Fig. 1b) while the material outside the FPZ behaves elastically.

In the present study, a modified version of the discrete fracture model originally developed by Munjiza et al. (1999) was employed. With this model, crack walls are assumed to coincide with the edges of the triangular finite elements and the relative crack wall displacements are evaluated using dedicated 4-noded crack elements, as illustrated in Fig. 1c. Depending on the local stress and deformation field, fractures can nucleate and propagate via mode I (i.e., opening mode), mode II (i.e., sliding mode) or mixed mode I–II.

Mode I fracture initiation and propagation is simulated through a cohesive crack model based on the theoretical model originally proposed for concrete by Hillerborg et al. (1976). As shown in Fig. 2a, the crack initiates when the crack tip opening, o, reaches a critical value, o_p, which corresponds to the intrinsic tensile strength of the rock, f_t. As the fracture propagates and the crack tip opening increases, the normal stress, σ, is assumed to decrease until a residual opening value, o_r, is reached and a stress-free surface is created.

Mode II fracture initiation and propagation is simulated by a slip-weakening model. As depicted in Fig. 2b, a tangential stress, τ, exists between the two fracture walls,

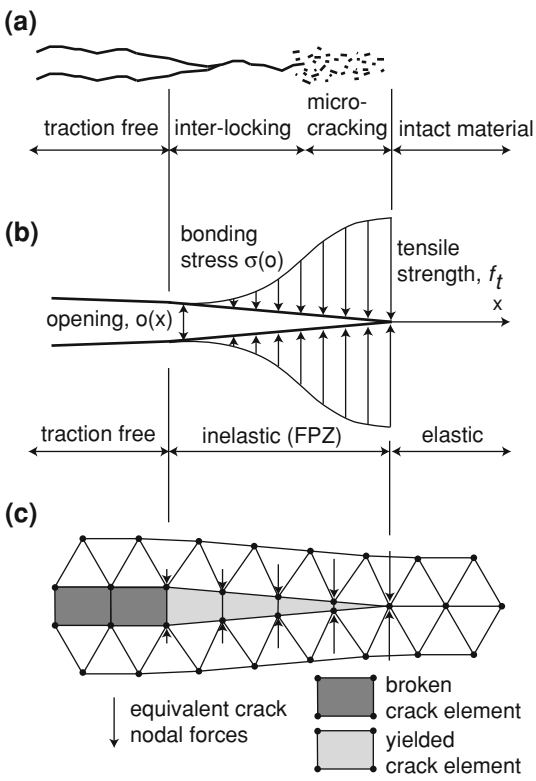

Fig. 1 **a** Conceptual model of tensile fracture in rock (after Labuz et al. (1985)), **b** theoretical FPZ model of Hillerborg et al. (1976), **c** FEM/DEM numerical model consisting of triangular elements and 4-noded crack elements

which is a function of the amount of slip, s, and the normal stress on the fracture. The critical slip, s_p, corresponds to the intrinsic shear strength of the rock, f_s, defined as

$$f_s = c + \sigma_n \tan \phi_i, \tag{1}$$

where c is the internal cohesion, ϕ_i is the intact material friction angle, and σ_n is the normal stress acting across the crack element. Upon undergoing the critical slip s_p, the tangential stress is gradually reduced to a residual value, f_r, which corresponds to a purely frictional resistance:

$$f_r = \sigma_n \tan \phi_f, \tag{2}$$

where ϕ_f is the fracture friction angle. In the current implementation of the crack element response (Fig. 2), the unloading path in the softening branch coincides with the loading path. Therefore, the model is strictly only valid for monotonic loading conditions.

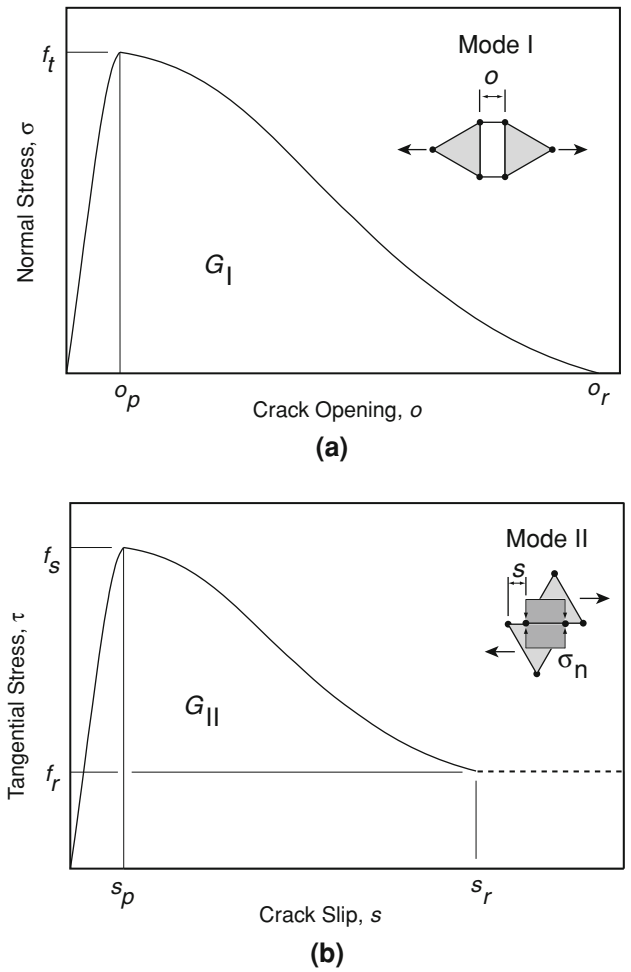

Fig. 2 Fracture model implemented in the Y-Geo FEM/DEM code: **a** FPZ model for mode I, **b** slip-weakening model for mode II. The shape of the curves in based upon experimental complete stress–strain curves obtained for concrete in direct tension (Evans and Marathe 1968). Further details can be found in Munjiza et al. (1999) and Mahabadi et al. (2012a)

For mixed mode fracturing, the rupture of a crack element is defined by the following coupling criterion between crack opening and slip:

$$\left(\frac{o - o_p}{o_r - o_p}\right)^2 + \left(\frac{s - s_p}{s_r - s_p}\right)^2 \geq 1. \tag{3}$$

The values of residual opening and slip depend on the tensile and shear strength and the mode I and mode II fracture energy release rates, G_I and G_{II}, for the material. The values of G_I and G_{II} are defined as:

$$G_I = \int_{o_p}^{o_r} \sigma(o)do \tag{4}$$

$$G_{II} = \int_{s_p}^{s_r} (\tau(s) - f_r)ds \tag{5}$$

3.3 Material Anisotropy

As part of this research project, the capabilities of the two-dimensional Y-Geo code were extended such that the mechanical response of anisotropic materials could be simulated. Details of the adopted approach are illustrated in the following subsections.

3.3.1 Anisotropy of Deformation

Like most argillaceous rocks, OPA is a distinctively bedded material with mechanical behaviour that is best described as transversely isotropic (Popp and Salzer 2007a). That is, the deformability of the rock can be considered isotropic within any plane normal to an axis of rotational symmetry coincident with the normal to the bedding plane orientation (Fig. 3a). Therefore, to describe the elastic response of OPA, a stress–strain constitutive law for transversely isotropic elastic solids was implemented in FEM/DEM. For such materials, there are five independent elastic constants (Ting 1996): E_1 and E_2 (=E_3) are the Young's moduli in the direction perpendicular, s_1, and parallel, s_2, to the bedding, respectively; ν_{12} (=ν_{13}) and ν_{23} are the Poisson's ratios that define the lengthening deformation in the directions s_2 and s_3 due to normal stresses in the directions s_1 and s_2, respectively; and G_{12} is the shear modulus in the (s_1, s_2) plane. The naming convention of Fig. 3b is used in the present work to identify the test specimens according to the direction of anisotropy.

3.3.2 Anisotropy of Strength

A large body of experimental evidence (e.g., Popp and Salzer 2007a; Bock 2009) clearly indicates that the mechanical strength of OPA during laboratory tests is

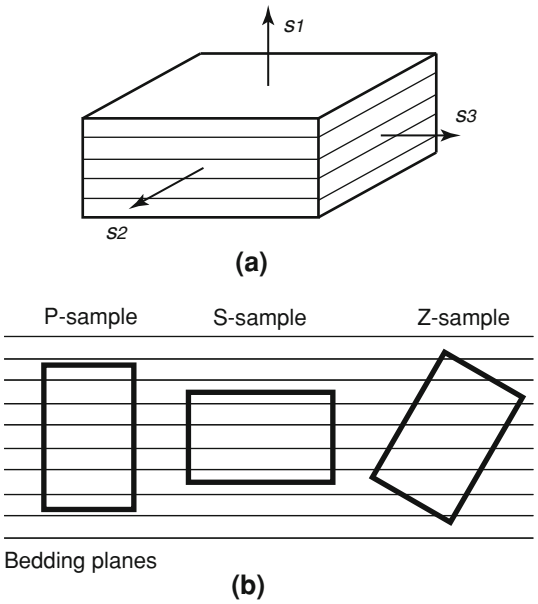

Fig. 3 **a** Conventional structural coordinates for a transversely isotropic material, **b** adopted naming convention of the test samples of Opalinus Clay

strongly direction-dependent. The maximum unconfined compressive strength value is generally obtained when samples are loaded in the direction perpendicular to the bedding (S-sample). A local maximum value, lower than the previous one, occurs when samples are loaded in the direction parallel to the layering (P-sample), while a substantial strength reduction is observed for loading angles between these two limiting cases. Similar strength response has been observed for other kinds of anisotropic rocks (Donath 1972).

To capture this characteristic behaviour in FEM/DEM, a discrete representation of material anisotropy was implemented. This approach follows that which was introduced by Potyondy and Cundall (2000) in a 2D bonded-particle code to simulate the mechanical response of gneissic tonalite and extended to 3D by Wanne (2002). With this approach, the anisotropy of strength is captured as an emergent property of a medium containing a distribution of pre-existing cracks aligned with the bedding planes without introducing any directional dependence in the crack element strength parameters. Since this procedure can be extended to the general case of multiple arbitrarily-oriented discontinuities, often referred to as a discrete fracture network (DFN), the resulting micro-mechanical model of OPA is referred to herein as the FEM/DEM-DFN model.

The newly-developed procedure involves populating a homogenous FEM/DEM model, representing the rock matrix, with a distribution of finite-length discontinuities to represent the bedding planes. This pattern of pre-existing cracks (i.e., DFN) is characterized by two groups of properties:

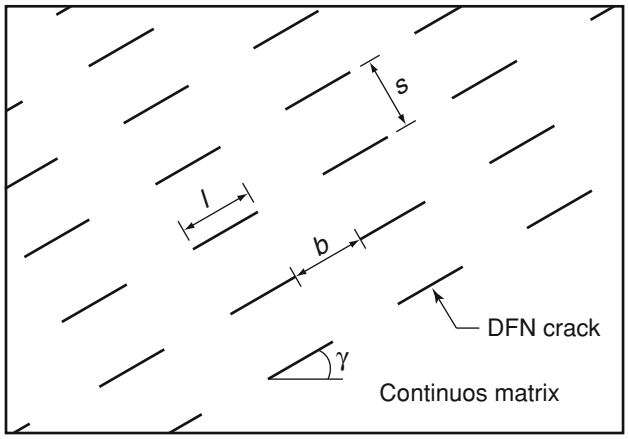

Fig. 4 Geometrical parameters characterizing the distribution of pre-existing cracks (DFN)

- DFN geometry. The DFN geometry is described by the following parameters (Fig. 4): fracture length, l, fracture spacing, s, fracture bridge length, b, and crack orientation, γ. Initial aperture and tangential slip are set to zero for all cracks.
- DFN mechanical properties. After all the cracks have been created, the following mechanical properties are specified for each discontinuity: friction angle, ϕ_f, and normal and tangential penalty coefficient, p_n and p_t, which represent normal and tangential stiffness, respectively (Munjiza 2004). All the DFN cracks are assumed to have zero cohesion and tensile strength.

The DFN property values are determined during the first step of the model calibration procedure as illustrated in Sect. 4.2.

4 Model Calibration

The FEM/DEM-DFN models were calibrated to averaged laboratory results; namely, uniaxial compression tests and indirect tension (Brazilian) tests reported by Bock (2009) for the shaly facies of the Mont Terri OPA. The model boundary conditions, calibration procedure, and results are discussed in the following subsections.

4.1 Geometry and Boundary Conditions

The two-dimensional laboratory-scale models included 35.8 × 17.4 mm rectangular specimens for the compression test and 29.7 mm diameter disc specimens for the Brazilian test. All the specimen cross-sections were assumed to be oriented perpendicular to the strike of the bedding planes. The direction of anisotropy was then varied by changing the DFN inclination such that loading conditions reported in Fig. 3b could be reproduced.

The specimens were discretized with triangular elements having an average edge size of 0.30 mm. Load was applied by means of two rigid triangular platens moving at a constant velocity of $v = 0.1$ m/s. Although this loading rate is much greater than that used in the laboratory tests, a sensitivity analysis of the modelling results to the loading rate revealed that simulated strengths approached constant values for loading rates smaller than approximately 0.25 m/s. An integration time step of 3×10^{-6} ms was used to solve the equations of motion for both specimen geometries. Input files for the FEM/DEM simulations were created using the Y-GUI software (Mahabadi et al. 2010).

4.2 Calibration Procedure and Input Parameters

Discrete element models synthesize the macroscopic behaviour of the material from the interaction of micro-mechanical constituents. As result, the measurements from standard laboratory tests cannot, in general, be directly used as input parameters. Instead, input parameters are determined through a calibration process, in which the emergent properties of the model are compared to the relevant measured response of the material (Potyondy and Cundall 2004). Although Mahabadi et al. (2012b) demonstrated that a micro-mechanical characterization of the investigated medium may reduce the number of input parameters requiring numerical calibration, such a procedure was not attempted for this study.

The following laboratory-scale properties were chosen to characterize the short-term response of OPA and were used as calibration targets for the FEM/DEM-DFN models: elastic modulus, E, Poisson's ratio, ν, uniaxial compressive strength, UCS, and indirect tensile strength, T. Since each of these properties exhibits a dependence upon the orientation of the material anisotropy, values corresponding to loading parallel (P-sample) and perpendicular (S-sample) to layering were considered. The input parameters required to reproduce these target values were obtained through an iterative process utilizing models of uniaxial compressive strength (UCS) tests and Brazilian disc (BD) tests. The main steps of this process proceeded as follows:

(i) Using the BD models, the average crack length in the DFN was adjusted to match the laboratory-measured anisotropy ratio of the indirect tensile strength, T_P/T_S. Given the ubiquitous nature of layering in OPA and the adopted element size (0.3 mm), an average crack spacing and bridge length of 1.0 mm were arbitrarily assumed.

(ii) Using the BD models, the material tensile strength, T, and mode I fracture energy, G_I, were varied until a good approximation of the indirect strength values, T_P and T_S, were obtained.

(iii) Using the UCS models, the material cohesion, c, and the mode II fracture energy, G_{II}, were adjusted to satisfactorily match the UCS values, UCS_P and UCS_S.

(iv) Returning to the BD models, the simulations were re-run using the parameters updated during step (iii).

The finalized geometric and mechanical parameters of the DFN are reported in Table 1. A uniform distribution was assumed for each geometric parameter. The specified mean crack orientation, with a range of ±5°, was selected to mimic the orientation of layering in the test specimens (Fig. 3b). For the remaining three parameters, a range equal to 10 % of the mean value was assumed. An average crack length of 2.0 mm was obtained through step (i) of the calibration process. This value yielded a ratio of crack length to bridge length of 2, which is approximately equal to the anisotropy ratio of the indirect tensile strength, T_P/T_S. Since the anisotropy of deformation was accounted for through the transversely isotropic elastic law applied to the deformable triangular elements (Sect. 3.3.1), the discrete fractures were assigned normal and tangential penalty values equal to those of the rock matrix. Zero tensile strength and cohesion were assumed for all fractures. A friction angle of 22° was selected based on the results of direct shear testing of bedding planes by Popp and Salzer (2007b).

The finalized mechanical and numerical parameters of the rock matrix are reported in Table 2. The values of the strength parameters for the rock matrix were obtained as the final result of step (ii), (iii) and (iv) of the calibration process, while the experimental values of the elastic constants measured by Bock (2009) were used directly as input for the transversely isotropic elastic model. Although the presence of 4-noded crack elements across the interfaces of triangular elements effectively reduces the stiffness of the model, this effect was minimized by selecting appropriate

Table 1 Geometrical parameters and mechanical properties of the discrete fracture network of the calibrated FEM/DEM-DFN model

Geometrical parameter	Mean value	Range
Crack inclination, γ (°)	Varying	±5.0
Crack spacing, s (mm)	1.0	±0.1
Crack length, l (mm)	2.0	±0.2
Bridge length, b (mm)	1.0	±0.1
Mechanical property	**Value**	
Normal contact penalty, p_n (GPa)	38	
Tangential contact penalty, p_t (GPa)	3.8	
Internal cohesion, c (MPa)	0	
Tensile strength, f_t (MPa)	0	
Friction angle, ϕ_f (°)	22	

values for the penalty coefficients. Following the recommendations of Mahabadi (2012), normal contact penalty, p_n, tangential penalty, p_t, and fracture penalty, p_f, values were set equal to 10×, 1× and 5× the maximum Young's modulus, respectively. The viscous damping coefficient, μ, was assigned a value according to Munjiza (2004), as:

$$\mu = 2h\sqrt{E\rho}, \tag{6}$$

which approximates the theoretical critical damping assuming a single element of size h behaves as a one-degree-of-freedom mass-spring-dashpot system. Nevertheless, preliminary analyses revealed a relatively low sensitivity of the model to the applied damping under the given loading rate. That is, dynamic effects due to the propagation of stress waves throughout the model had only minor effects on the overall strength and deformation response of the samples.

4.3 Calibration Results

Table 3 compares the emergent properties of the calibrated FEM/DEM-DFN models with the experimental values of OPA reported by Bock (2009) which were used as calibration targets.

Table 2 Mechanical and numerical parameters for the rock matrix of the calibrated FEM/DEM-DFN model

Parameter	Value
Triangular elements	
Bulk density, ρ (kg/m^3)	2,330
Young's modulus perpendicular to bedding, E_1 (GPa)	1.3
Young's modulus parallel to bedding, E_2 (GPa)	3.8
Poisson's ratio parallel to bedding, v_{12} (−)	0.35
Poisson's ratio perpendicular to bedding, v_{23} (−)	0.25
Shear modulus, G (GPa)	0.9
Viscous damping coefficient, μ (kg/m s)	1.79e3
Crack elements	
Tensile strength, f_t (MPa)	0.65
Internal cohesion, c (MPa)	4.5
Friction angle of intact material, ϕ_i (°)	22
Friction angle of fractures, ϕ_f (°)	22
Mode I fracture energy release rate, G_I (J/m^2)	7
Mode II fracture energy release rate, G_{II} (J/m^2)	35
Platen-sample friction coefficient, k (−)	0.1
Normal contact penalty, p_n (GPa m)	38
Tangential contact penalty, p_t (GPa/m)	3.8
Fracture penalty, p_f (GPa)	19
Critical crack opening, o_p (μm)	0.021
Residual crack opening, o_r (μm)	32
Critical crack slip, s_p (μm)	0.142
Residual crack slip, s_r (μm)	23

The indirect tensile stress, σ_t, in the BD specimens as function of the platen vertical displacement, δ_v, was calculated from the platen reaction forces, according to the ISRM suggested method (Bieniawski and Hawkes 1978). As shown in Fig. 5a, the response of both samples was elastic-brittle with complete loss of strength immediately after reaching the peak strength values. Peak values of 1.20 and 0.78 MPa were obtained for the P- and S-sample, respectively. These values are considered a good match to the respective average experimental values of 1.3 and 0.67 MPa.

Figure 6 depicts the simulated and experimentally observed fracture patterns of the BD tests. As expected, the simulated failure mode was mainly given by brittle tensile splitting along the vertical loading path. For the P-sample, shear fractures were observed in proximity to the loading platens due to the induced compressive stress field. Although this additional failure mechanism was responsible for the oscillations of the indirect tensile stress that can be observed in Fig. 5a, a simulation whereby the cohesion was artificially increased to induce tensile failure of the specimen revealed that its influence on the indirect tensile strength value, f_{tP}, was minimal.

Figure 5b shows the plot of axial stress, σ_1, versus axial strain, ε_1, and lateral strain, ε_3, for the UCS simulations. The response of both samples is approximately linearly-elastic until the failure stress is reached and a sudden and complete loss of strength is simulated. Simulated unconfined compressive strength values were equal to 11.9 and 14.0 MPa for the P- and S-sample, respectively. These values were in good agreement with the respective experimental values of 11.6 and 14.9 MPa. As reported in Table 3, the numerical response of the UCS models satisfactorily matched the elastic experimental behaviour in terms of axial and lateral deformation. As discussed previously in Sect. 3.2, the slight discrepancy between numerical and experimental values was due to the artificial compliance introduced by the 4-noded crack elements.

As illustrated in Fig. 7a, the numerical response of OPA under unconfined compressive load is characterized by substantially different failure mechanisms when loaded in the direction parallel (P) or perpendicular (S) to the bedding planes. The macroscopic failure mode of the P-sample is given by axial splitting due to fractures initiating from the tips of the DFN cracks, while the failure mode of the S-sample consists of shear fractures, propagating through the rock matrix and inclined at approximately 60°, combined with some tensile fracturing. As can be observed in Fig. 7b, the simulated fracture patterns are in excellent agreement with those typically observed in the laboratory.

Table 3 Comparison between the mechanical laboratory properties of the Mont Terri Opalinus Clay from Bock (2009) and the emergent properties of the FEM/DEM-DFN model

Macroscopic mechanical property	P-sample		S-sample	
	experimental value	FEM/DEM-DFN result	experimental value	FEM/DEM-DFN result
Elastic modulus, E (GPa)	3.8 ± 1.5	3.6	1.3 ± 0.7	1.3
Poisson's ratio, ν (−)	0.35	0.39	0.25	0.27
Uniaxial compressive strength, *UCS* (MPa)	11.6 ± 3.9	11.9	14.9 ± 5.1	14.0
Indirect tensile strength, T (MPa)	1.30	1.13	0.67	0.71

4.4 Analysis of Failure Process

4.4.1 DFN Orientation and Anisotropy of Strength

For indirect tensile loading conditions (BD model) (Fig. 6a), the DFN orientation effectively varies the area in which tensile strength can be mobilized. Hence, the tensile strength anisotropy ratio was controlled by the ratio of crack length to rock bridge length in the DFN. Furthermore, numerical results show that the bedding planes tend to arrest crack propagation and off-set the fracture trajectory in the P-sample, but represent the preferred path of new tensile cracks in the S-sample.

For unconfined compressive loading conditions (UCS model) (Fig. 7a), the orientation of the DFN directly influences the failure mode of the specimen. In the P-sample, the tensile stress induced by the Poisson's effect in the direction perpendicular to the maximum compressive stress, σ_1, causes the nucleation and propagation of extensile fractures from the tips of the pre-existing cracks. This observation is confirmed by the analysis of the fracture mode distribution reported in Fig. 8, which reveals that 51 % of the UCS P-sample fractures are indeed mode I. Upon propagation of sub-vertical fractures, kinking and buckling of compressed layers can be observed with subsequent lateral ejection of rock slabs. It is noteworthy that a similar buckling failure mechanism has been observed in the laboratory during hollow cylinder experiments on OPA (Labiouse 2012) and in situ around boreholes at the Mont Terri URL (Vietor et al. 2012). In the S-sample, the macroscopic failure mechanism is given by shearing. Although mode II fracturing is predominant, a non-negligible percentage of mode I fractures (33 %) is simulated. These

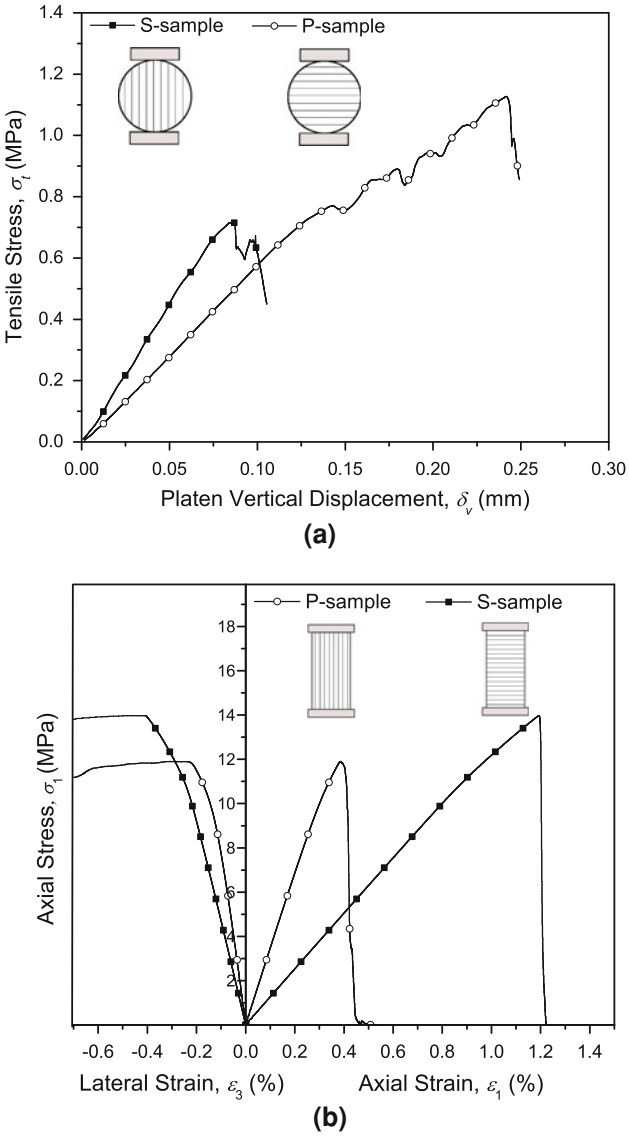

Fig. 5 **a** Tensile stress, σ_t, versus platen vertical displacement for the BD P- and S-samples, **b** axial stress, σ_1, versus axial strain, ε_1, and lateral strain, ε_3, for the UCS P- and S-sample

numerical results tend to confirm the importance of extensional fracturing in the brittle failure process of samples of OPA under unconfined compression as described and experimentally verified by Amann et al. (2011).

4.4.2 Brittle Failure Process in Unconfined Compression

The simulated failure process of OPA in uniaxial compression can be described with reference to the critical stress levels and behaviour stages that are typical of brittle rocks (Bieniawski 1967). According to Martin (1997), five stages can be identified: (1) closure of micro-cracks and crushing of asperities, (2) linear elastic behaviour, (3) onset of dilation and stable crack propagation, (4) unstable crack

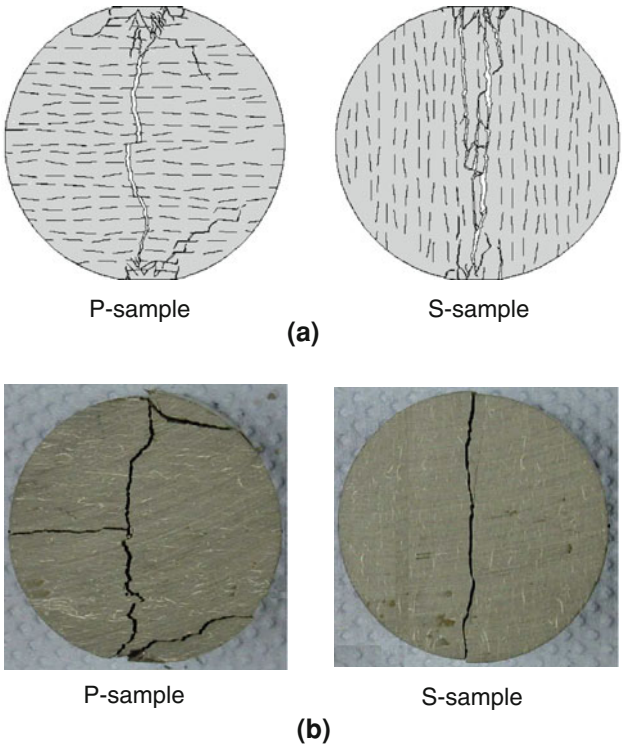

Fig. 6 Fracture patterns of the BD tests: **a** FEM/DEM-DFN simulations, **b** typical experimental observations (Source: Jahns (2010))

growth, and (5) brittle post-peak. The onset of linear elastic behaviour is marked by the crack closure stress threshold, σ_{CC}. The lower and upper limits of stage 3 are defined by the crack initiation and crack damage stress thresholds, σ_{CI} and σ_{CD}, respectively, while stage 4 falls between σ_{CD} and the UCS value. Analysis of the brittle failure process is performed on the stress–strain response of the UCS P-sample reported in Fig. 9 and is discussed below with reference to the five stages listed above. Note that an analogous behaviour was simulated for the S-sample.

The presence of the low-stiffness non-linearity at low strain levels (i.e., stage 1) was first observed in OPA by Bock 2001 and is associated with the breakage of diagenetic bonds following the sample recovery process (Corkum and Martin 2007). The proposed FEM/DEM-DFN model has no means to account for this non-linear effect neither at the matrix level (i.e., continuum) nor at the bedding plane level (i.e., DFN). Since the triangular elements are assumed to follow a linear elastic behaviour and the DFN discontinuities are assumed to have zero aperture and the stiffness of the matrix, no "closure effect" can be reproduced.

The linear-elastic stage (i.e., stage 2), typically observed in samples of OPA under unconfined compression, is captured in the simulation by the elastic deformation of the rock matrix (from point O to A-A' in Fig. 9).

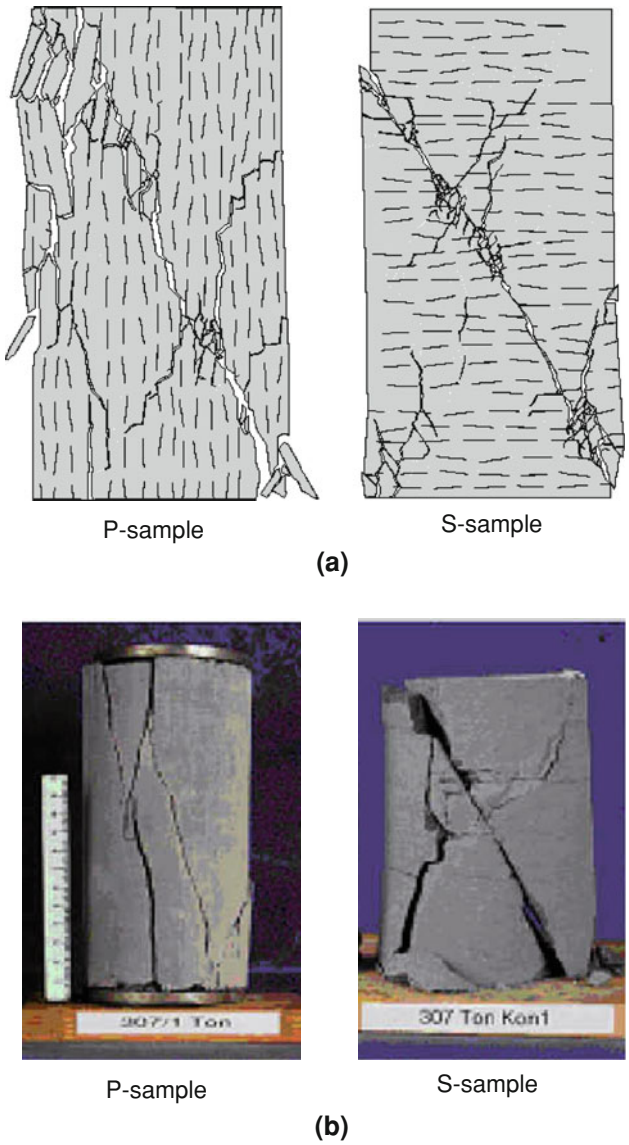

Fig. 7 Fracture patterns of the UCS tests: **a** FEM/DEM-DFN simulations (note the buckling of layers and ejection of rock slabs on the left side of the specimen), **b** typical experimental observations (Source: Popp et al. (2008))

A thorough analysis of stage 3 and 4 for UCS S-samples of OPA can be found in Amann et al. (2011). Based on acoustic emission measurements and analysis of the stress–strain behaviour, crack initiation and crack damage thresholds were identified at 30 % and approximately 70 % of the rupture stress, respectively. In the simulated stress–strain response reported in Fig. 9, axial and lateral strains start to deviate from linearity at 70 % (point A) and 55 % (point A') of the UCS value, respectively. As revealed by the count rate of yielded crack elements, this loss of linearity is related to the onset of softening at the crack element level. The linearity in the lateral strain is lost first because crack elements tend to first yield in tension in the direction

parallel to the maximum principal stress (i.e., mode I). Although no actual fracturing is reproduced at this stage, in the framework of the fracture model implemented in FEM/DEM, the simulated crack element softening is representative of the micro-cracking that occurs in the FPZ (Fig. 1). As the load is increased, the count rate of yielded crack elements increases and damage starts to accumulate in the sample resulting in a non-linear pre-peak response. Therefore, the stress level associated with point A can be interpreted as the equivalent of the crack damage stress threshold, σ_{CD}.

It is evident that the model cannot capture the stage of stable crack propagation (stage 3), between the crack initiation and crack damage thresholds, that typically causes the lateral strain and volumetric strain response to deviate from linearity at about 30–50 % of the uniaxial rupture stress (Brace et al. 1966). This stage has been related to the nucleation of mode I cracks due to local tensile stress fields induced by grain-scale heterogeneities (Tapponnier and Brace 1976). Although numerous sources of micro-scale heterogeneities have been observed in the OPA, including carbonate bioclasts, pyrite, sandy nodules and calcite veins (Klinkenberg et al. 2009), the rock matrix was assumed to be homogenous in the present study. As other micro-mechanical models of rocks have clearly demonstrated (e.g., Tang and Kaiser 1998; Diederichs 2000; Lan et al. 2010; Mahabadi 2012) it is likely that the explicit incorporation of material heterogeneity into the FEM/DEM-DFN model will overcome this limitation and provide a more accurate simulation of the pre-peak brittle failure process.

Finally, as the load is further increased, the accumulated damage in the sample leads to the failure of crack elements and the sudden drop in stress (Point B). This brittle post-peak response is typical of stage 5 and is characterized by the macroscopic fracture pattern depicted in Fig. 7a.

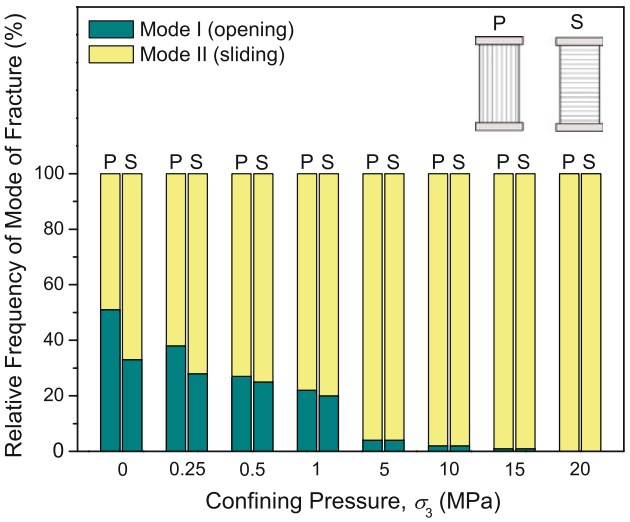

Fig. 8 Relative frequency of fracture mode for the P- and S-sample at increasing confining pressures, σ_3

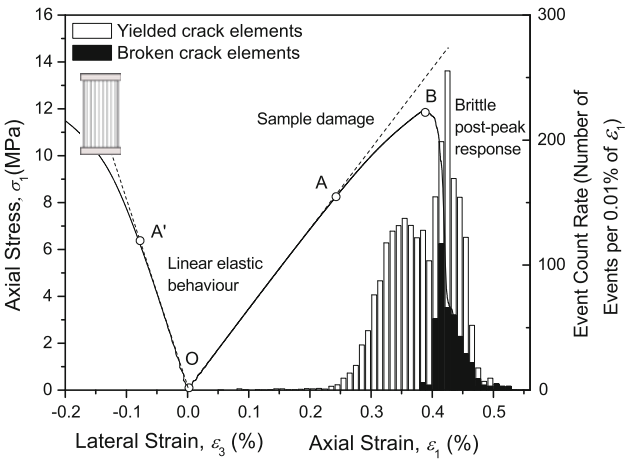

Fig. 9 Axial stress, σ_1, versus axial strain, ε_1, and lateral strain, ε_3, for the UCS P-sample and associated count rate of yielded and failed crack elements as a function of axial strain, ε_1

5 Model Validation

The calibrated FEM/DEM-DFN model was validated by simulating the effect of confinement and anisotropy direction on the failure process of OPA under compressive loading. The material properties and numerical parameters obtained as a result of the calibration process were left unchanged for this validation. Biaxial loading conditions were obtained by applying a lateral pressure to the specimen boundaries. Numerical results are compared to published experimental findings on OPA and other anisotropic rocks.

5.1 Effect of Confining Pressure

5.1.1 Results

Figure 10 shows the deviatoric stress, σ_1–σ_3, as a function of the axial strain, ε_1, at increasing confining pressures, σ_3, for the P- and S-sample, respectively. For both specimens, the mobilization of friction increases the deviatoric stress at failure as the confining pressure increases. A transition from brittle to ductile post-peak behaviour can be observed at a confining pressure of approximately 7.5 MPa for both samples. This change of response corresponds well with the results of biaxial compression tests on OPA reported by Salager et al. (2010), in which a ductile post-peak was observed in S-samples for $\sigma_3 \geq 10$ MPa.

The failure modes of the P- and S-sample are depicted in Fig. 11a, b, respectively. Under unconfined conditions

($\sigma_3 = 0$ MPa), the P-sample exhibits axial splitting and buckling of layers. As the confinement is increased ($0.5 \leq \sigma_3 \leq 1$ MPa), longitudinal fractures tend to be suppressed in favour of a well-defined shear plane inclined at about 57° from the horizontal. For $\sigma_3 = 5$ MPa, two conjugated shear fractures can be clearly identified. For higher confinements ($\sigma_3 \geq 10$ MPa), the damage pattern consists mainly of a network of short cracks. The S-sample exhibits fracture behaviour similar to the P-sample for confinement values $\sigma_3 \geq 1$ MPa. However, for very low confinements a combination of shear and tensile fracturing is simulated without the characteristic axial splitting and buckling of layers of the P-sample. This overall variation of macroscopic fracture response as a function of the applied confinement is in agreement with the mechanisms described by Jaeger and Cook (1976) and Paterson and Wong (2004).

An example of progressive material breakdown and horizontal displacement field evolution is shown in Fig. 12 for the P-sample with $\sigma_3 = 15$ MPa. The appearance of the first macroscopic crack at $\varepsilon_3 = 1.5$ % is followed by the nucleation throughout the sample of short shear cracks inclined at about ±50° from the horizontal ($\varepsilon_3 = 2.5$–3.5 %). Further increase of applied strain ($\varepsilon_3 = 4.5$–5.5 %) leads to the formation of two major through-going fracture planes. The associated horizontal displacement field evolves from lateral contraction at low axial strain levels ($\varepsilon_3 < 2.5$ %) due to the applied confining pressure to lateral expansion and dilation for higher applied deformation. Also, sample barrelling becomes more evident as damage accumulates into the model.

Simulated failure envelopes of the P- and S-samples are plotted in Fig. 13. It is noted that for confinement values $\sigma_3 < 2$ MPa the strength of the P-sample is lower than that of the S-sample, while for $\sigma_3 \geq 2$ MPa the opposite response is simulated.

This characteristic variation of strength response is highlighted by the plot of the anisotropy parameter K_1, defining the ratio between the deviatoric stress at failure in the direction parallel and perpendicular to the bedding,

$$K_1 = \frac{(\sigma_1 - \sigma_3)_{//}}{(\sigma_1 - \sigma_3)_{\perp}}, \tag{7}$$

as a function of the confinement, σ_3. As depicted in Fig. 14, K_1 increases from 0.85 to 1.15 as σ_3 increases from 0 MPa (i.e., unconfined conditions) to 20 MPa and is equal to 1 for a σ_3 value of about 2.0 MPa. This simulated behaviour is confirmed by the experimental evidence on OPA reported by Popp et al. (2008) and Bock (2009).

Lastly, the quantitative comparison between numerical failure envelopes and experimental values compiled from Popp et al. (2008) and Jahns (2010) (Fig. 15) indicates that the FEM/DEM-DFN models correctly reproduce the average mechanical response of P- and S- samples of OPA.

5.1.2 *Non-Linear Behaviour and Brittle-Ductile Transition*

Overall, the results of the biaxial test models demonstrate a good agreement with published experimental findings in terms of the stress–strain response, fracture pattern, and failure envelope.

Correctly capturing the response of the material under unconfined or moderately confined conditions is crucial when assessing the near-field stability of underground

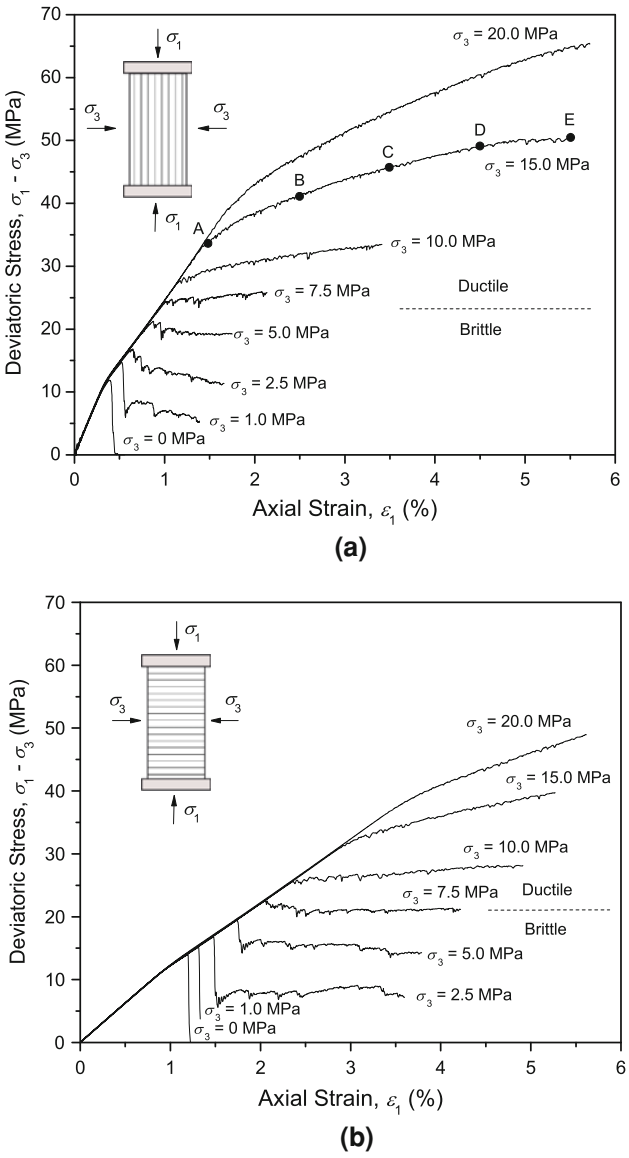

Fig. 10 Deviatoric stress, σ_1–σ_3, vs. axial strain, ε_1, at increasing confining pressure values, σ_3, for the **a** P-sample and **b** S-sample. Fracture pattern associated with point *A* to *E* in **a** is illustrated in Fig. 12

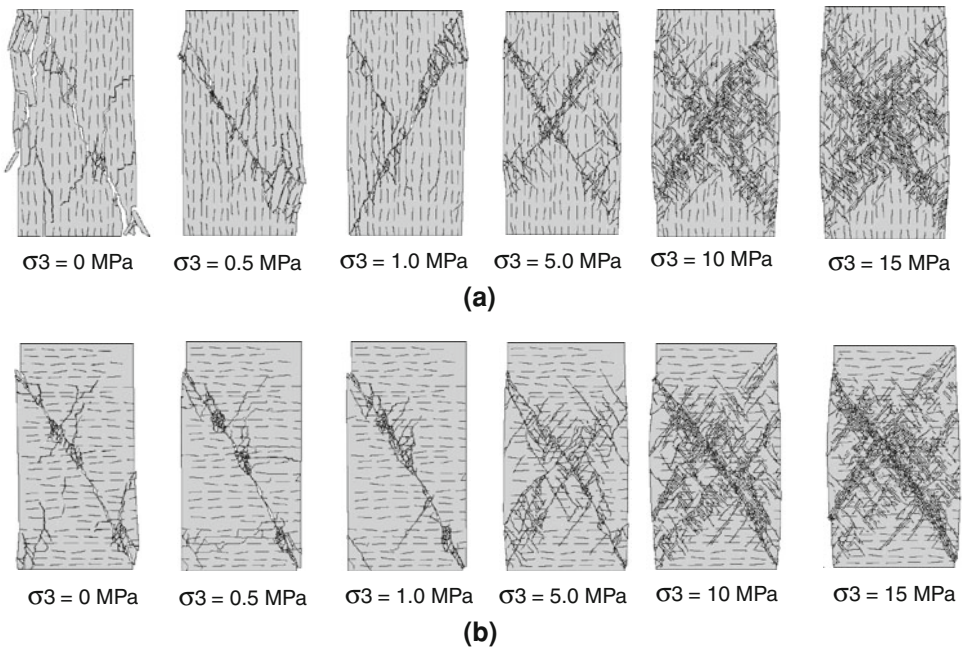

Fig. 11 Simulated fracture patterns of the **a** P-sample and **b** S-sample for increasing confining pressure values, σ_3

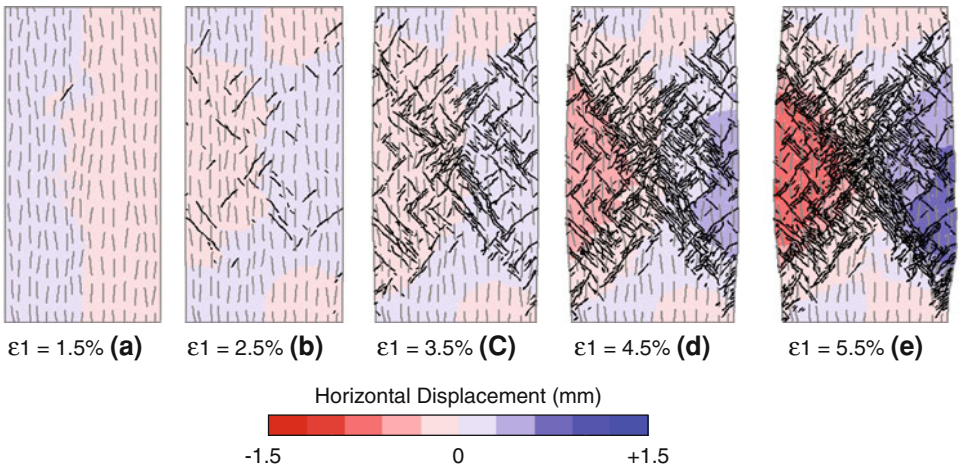

Fig. 12 Fracture pattern and horizontal displacement evolution of the P-sample ($\sigma_3 = 15$ MPa) at axial strain levels corresponding to point *A* to *E* on the associated stress–strain curve of Fig. 10

excavations (Diederichs 2003). Experimental data recently published by Amann et al. (2012), relative to biaxial tests on S-samples of OPA, show that a bi-linear or S-shaped (Kaiser and Kim 2008) failure criterion should be used to correctly capture the effect of the change in fracture mechanism, from tensile to shear dominated, as the confinement increases.

Although the numerical results relative to the S-sample do not show any non-linearity over the entire range of σ_3 (Fig. 13), the failure envelope of the P-sample clearly exhibits a concave downwards shape in the stress range 0 MPa $\leq \sigma_3 \leq$ 2.5 MPa. This non-linear behaviour can be explained by considering the fracture mode distribution as a function of the applied confinement (Fig. 8). In the P-sample, mode I fracturing, induced at low confinement by the preferably oriented DFN, contributes to the rupture of the sample. This fracturing occurs before the shear strength of the material is fully mobilized. As the confinement is increased, tensile fracturing is suppressed in favour of shearing, resulting in a linear Coulomb-type failure envelope. As illustrated in Fig. 16, this behaviour manifests itself as a variation of the orientation of the failed crack elements, which from sub-vertical tend to align along two inclined planes of failure. In contrast, the lower percentage of mode I fractures in the S-sample does not seem to have any notable effect on the response of the material. As a result, a Mohr–Coulomb type of behaviour is observed.

As previously discussed in Sect. 4.4, it is possible that the introduction of micro-scale heterogeneities (either in strength or in stiffness) would allow the grain-scale extensional fractures that have been associated with the

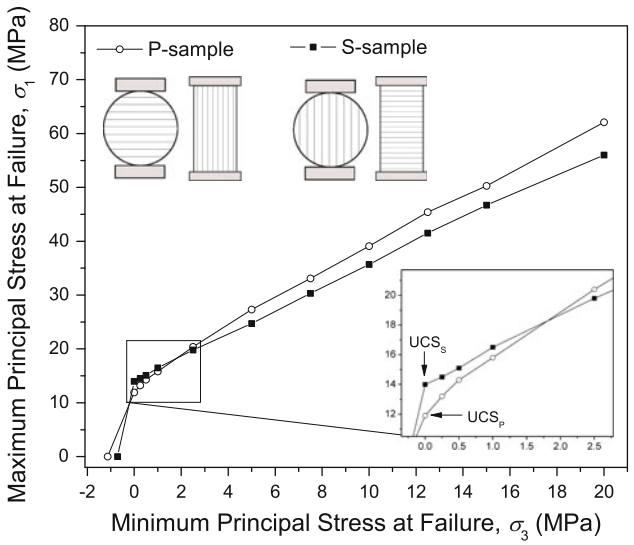

Fig. 13 Simulated failure envelopes of the **a** P-sample and **b** S-sample

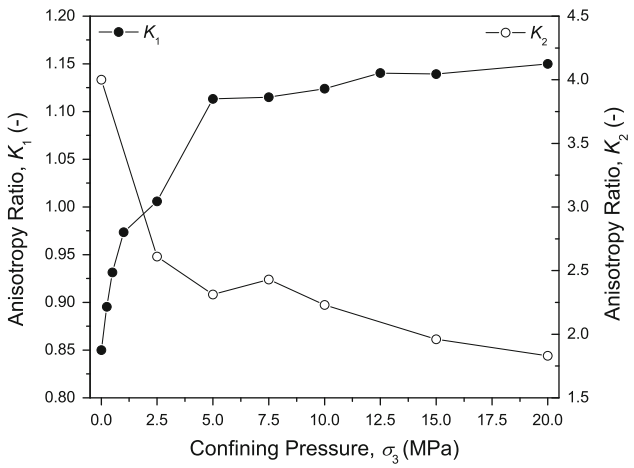

Fig. 14 Plot of the anisotropy ratios K_1 and K_2, defined by Eqs. (7) and (8), respectively, as a function of the applied confinement, σ_3

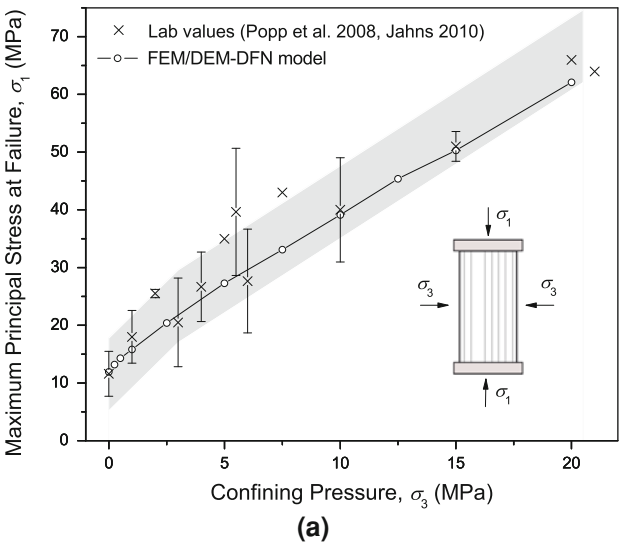

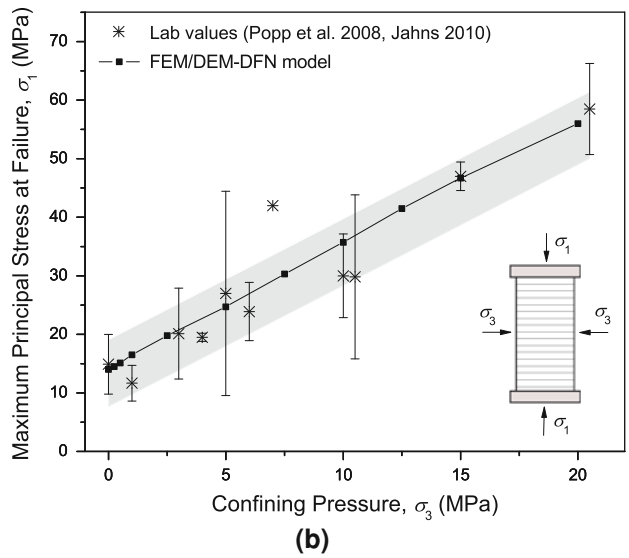

Fig. 15 Comparison of simulated failure envelopes with experimental values compiled from Popp et al. (2008) and Jahns (2010). **a** P-sample. The shaded area represents the interval calculated by bi-linear fitting of average experimental values ± standard deviation, in the range 0 MPa $\leq \sigma_3 \leq$ 2.5 MPa and 2.5 MPa $\leq \sigma_3 \leq$ 20 MPa. **b** S-sample. The shaded area represents the interval calculated by linear fitting of average experimental values ± standard deviation. Error bars are calculated using the standard deviation of experimental values at different confining pressures, σ_3

brittle failure process in OPA to be captured (Amann et al. 2011). Consequently, the experimentally observed non-linear strength behaviour of S-samples may also be captured.

The simulated transition of material behaviour from brittle to ductile assumes an increasing importance as the excavation depth increases. The impact of a brittle-ductile transition on the EDZ formation is two-fold. Firstly, as can be observed in Fig. 10, the material can sustain increasingly higher strain with increasing load bearing capacity (i.e., strain hardening). Secondly, a variation of fracture pattern, which directly affects the hydraulic properties in the EDZ, may be expected. In particular, the response of the material ceases to involve marked strain localization (i.e., brittle fracturing) in favour of a more pervasive and uniformly distributed deformation field, as shown in Fig. 11.

5.2 Effect of Specimen Anisotropy Orientation

5.2.1 Results

The simulated values of uniaxial compressive strength, *UCS*, and elastic modulus, *E*, for different loading angles, θ, are plotted in Fig. 17a. As the loading angle increases,

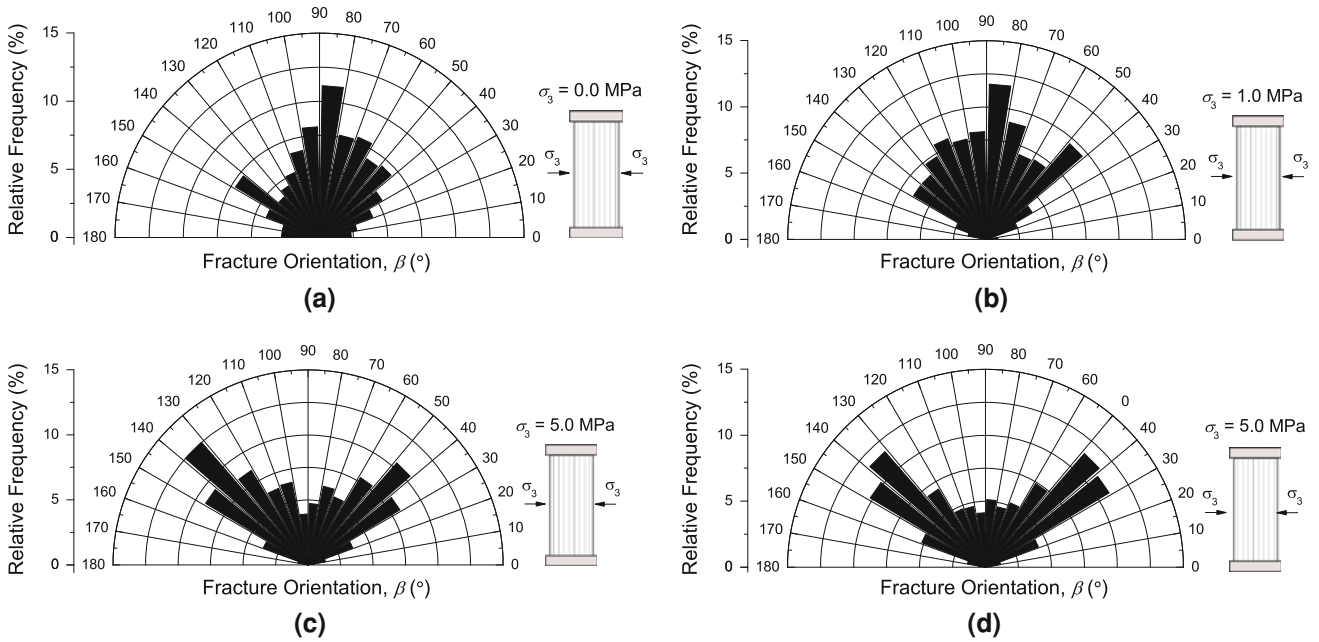

Fig. 16 Rosette plots of the relative distribution of failed crack elements orientation for the P-sample at confining pressures, σ_3, equal to **a** 0 MPa **b** 1 MPa **c** 5 MPa and **d** 15 MPa

the *UCS* first decreases from the P-sample value of 11.9 MPa (UCS_P) to a minimum value of 3.5 MPa for $\theta = 45°$, and then increases again to reach 14.0 MPa (UCS_S). That is, the simulated strength response exhibits the characteristic concave upwards, and parabolic in form, curve that has been typically observed in OPA (Naumann et al. 2007), other shales (McLamore and Gray 1967; Niandou et al. 1997), and anisotropic metamorphic rocks (Donath 1972).

The numerical results corresponding to $\theta = 30°$ show a 65 % reduction in strength with respect to UCS_P. This reduction is in agreement with the 50 and 80 % reduction observed in unconfined or moderately confined compression tests (Naumann et al. 2007; Jahns 2010). The deformation response as a function of the anisotropy direction is characterized by a decreasing elastic modulus with the loading angle varying from the P-sample value ($E_P = 3.6$ GPa) to the S-sample value ($E_S = 1.3$ GPa). Again, this behaviour is consistent with what observed in OPA (Salager et al. 2010) and other transversely isotropic rocks (Niandou et al. 1997).

To analyze the influence of confinement on the strength anisotropy of OPA, the ratio K_2 of the maximum to minimum deviatoric stress at failure was calculated:

$$K_2 = \frac{(\sigma_1 - \sigma_3)_{\text{Max}}}{(\sigma_1 - \sigma_3)_{\text{Min}}}. \quad (8)$$

As can be observed in Fig. 14, a decay of K_2 from the unconfined compression value of 4.0 is simulated for increasing confining pressures. Qualitatively, this response is consistent with experimental results of Naumann et al. (2007) for OPA and of Niandou et al. (1997) for the Tournemire Shale.

5.2.2 *Fracture Coalescence and Material Anisotropy*

The results illustrated above further validate the numerical model beyond the cases where specimens are compressed in the direction parallel or perpendicular to the bedding planes (Sect. 4.3, 5.1). As expected, the modulus anisotropy follows directly from the assumed constitutive law for the triangular elements and therefore is not discussed any further. However, the strength anisotropy emerges from a complex mechanical behaviour involving the interaction of newly generated fractures and pre-existing DFN cracks (Fig. 18) and thereby deserves a more thorough discussion.

Conventionally, the variation of strength with respect to the loading angle has been accounted for using discontinuous plane of weakness models (e.g., Jaeger and Cook 1976; Hoek and Brown 1980; Duveau et al. 1998). These conventional models use separate failure criteria to independently characterize the strength of the rock matrix and of the bedding planes. In contrast, with the FEM/DEM-DFN approach, the anisotropy of strength is captured by the variation of rupture mechanism induced by the interaction of the DFN with the rock matrix. Since no clear distinction between failure of the matrix and of bedding planes is made, a smooth transition in the strength response with loading angle is reproduced (Fig. 17a).

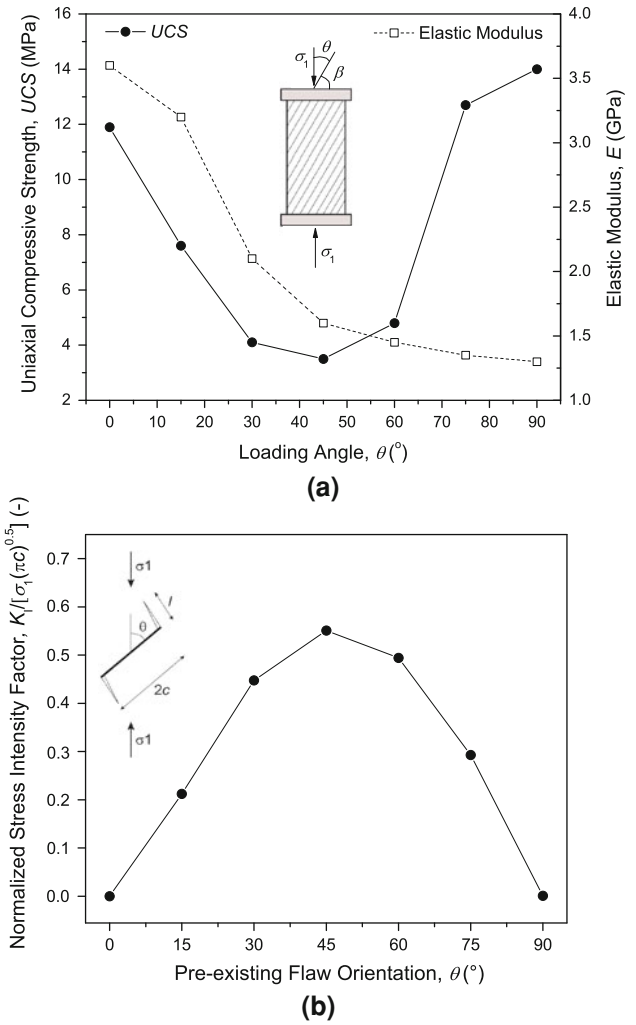

Fig. 17 **a** Simulated uniaxial compressive strength value, *UCS*, and elastic modulus, *E*, plotted as a function of the loading angle, θ, for the UCS Z-samples. **b** Normalized mode I stress intensity factor vs. inclination of the pre-existing flaw, θ, according to the solution of the sliding crack model proposed by Horii and Nemat-Nasser (1986) for the case of $l/c = 0.01$, where l is the wing crack length and $2c$ the pre-existing flaw length, and zero friction

For loading orientations $0° \leq \theta \leq 15°$, failure of the sample is induced by the extension of the bedding planes according to the process described for the UCS P-sample (Sect. 4.4). For loading orientations $75° \leq \theta \leq 90°$, failure occurs as a combination of shearing and extensional fracturing of the rock matrix as discussed for the UCS S-sample. For intermediate loading angles $15° < \theta < 75°$, a macroscopic shear failure can be observed resulting from the coalescence of the DFN cracks, which undergo mode I propagation from their tips.

This variation in behaviour can be explained using the basis of the theory of brittle failure of hard rock. According to the sliding crack model (Brace and Bombolakis 1963; Kemeny and Cook 1986), in a compressive stress field the surfaces of a pre-existing linear flaw tend to slide past each other inducing tensile failure of the rock at the crack tips. This initial tensile failure is followed by the propagation of two fractures, commonly referred to as wing cracks. The wing cracks initiate at an angle to the pre-existing crack and tend to align themselves in a direction parallel to the maximum principal stress. If a multitude of preferably oriented cracks are considered, such as in the FEM/DEM-DFN model, coalescence of the pre-existing cracks results in a characteristic step-path failure surface. The validity of this basic mechanism of fracture coalescence has been confirmed by several experimental and numerical studies (e.g., Bobet and Einstein 1998a, b; Tang and Kou 1998; Tang et al. 2001; Vesga et al. 2008; Yan 2008).

The analytical solution of the sliding crack model using linear elastic fracture mechanics principles can provide a qualitative explanation for the simulated variation of strength as a function of the DFN orientation. If failure of the specimen is assumed to be controlled by mode I crack initiation from the tips of pre-existing flaws, the strength of the specimen is ultimately dependent upon the mode I stress intensity factor, K_I, and the fracture toughness of the material, K_{IC}. Figure 17b shows the variation of K_I as a function of the pre-existing flaw angle, θ, calculated according to the solution of Horii and Nemat-Nasser (1986) for the case of a ratio of wing crack length to flaw length, l/c, equal to 0.01 and zero friction. It can be noticed that the variation of K_I with θ follows a curve that is approximately symmetric (with respect to the horizontal axis) of the *UCS* curve illustrated in Fig. 17a. Hence, being that the fracture toughness of the rock matrix is constant, flaw orientations (i.e., DFN) associated with higher K_I values are characterized by tensile crack propagation at lower compressive stress levels therefore resulting in lower *UCS* values of the specimen.

As shown in Fig. 18b, the introduction of confinement strongly affects the failure mode of the inclined samples and consequently the mechanism by which the strength anisotropy is captured by the FEM/DEM-DFN model. As described above, under unconfined compressive loading conditions, the strength anisotropy is dictated by the formation of wing cracks followed by tension-type fracture coalescence. However, under biaxial loading, tensile fracturing is suppressed and the coalescence of the DFN cracks is due to internal shearing. Therefore, as the confinement is increased, the simulated strength anisotropy is governed by the reduced shear strength that can be mobilized in the direction parallel to layering along the cohesion-less DFN discontinuities.

6 Mesh Sensitivity of the FEM/DEM Model

The sensitivity of a FEM/DEM model to the mesh element size and edge orientation arises from the assumptions

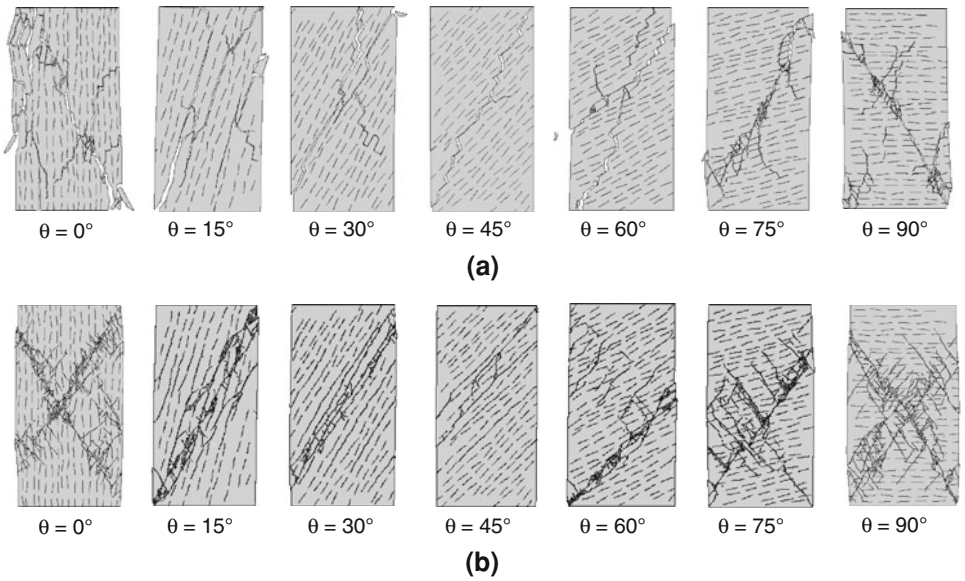

Fig. 18 Simulated fracture patterns of the **a** UCS test and the **b** 5 MPa confined biaxial compression test for different layering orientations

inherent in the adopted cohesive crack model (Sect. 3.2). To accurately represent the bonding stress close to the crack tip, the element size must be much smaller than the length of the FPZ (Fig. 1), defined as the distance from the crack tip to the point where the maximum cohesive strength (i.e., f_t or f_s) is attained (Munjiza and John 2002). The length of the FPZ, l_{FPZ}, can be analytically estimated using the following relationship valid for mode I fracturing (Hillerborg et al. 1976):

$$l_{\mathrm{FPZ}} = E\frac{G_{\mathrm{I}}}{f_{\mathrm{t}}^2}. \tag{9}$$

Using the parameters reported in Table 2 for OPA, l_{FPZ} values of 22 and 64 mm are calculated for $E = E_1$ and $E = E_2$, respectively. Although the exact minimum number of cohesive elements required in the FPZ is not well established, 3–10 elements have generally provided accurate results (Turon et al. 2007). Therefore, the adopted average element size of 0.3 mm, which results in at least 73 elements distributed in the FPZ, should provide an accurate representation of the stress and strain field in the vicinity of crack tips.

However, the simulated failure process of OPA samples in compression is due to a combination of mode I and mode II fracturing together with multiple interactions between newly-created and pre-existing discontinuities. That is, the simulated failure conditions are more complex than the pure opening mode upon which the above discussion is based. Therefore, the element size sensitivity of the FEM/DEM model was further investigated by simulating the response of the UCS P-sample for mesh refinements ranging between 0.2 and 0.4 mm. As shown in Fig. 19, the peak strength appears to converge with decreasing element size, which is in agreement with the previous theoretical analysis. Due to excessively long run times, it was not possible to simulate mesh resolutions finer than 0.20 mm. The adoption of smaller element size not only results in a rapid growth of the total number of elements (Fig. 19) but also requires smaller time step sizes to satisfy the stability condition of the explicit time integration scheme of FEM/DEM. Conversely, element sizes greater than 0.40 mm could not be used due to the adopted average spacing value of the DFN cracks (1.0 mm).

The mesh topology sensitivity of the cohesive element approach results from the restriction of crack nucleation and growth to the edges of the triangular elements. Although this approach aims at simulating fracturing without any a priori assumption regarding the fracture trajectory, a certain mesh bias is induced by the fact that the direction of crack propagation is not entirely free but restricted to a limited number of predefined angles. To minimize the constraint imposed by the mesh topology on the model behaviour, randomly discretized meshes should be used in place of regularly discretized ones (Tijssens et al. 2000; Mahabadi 2012). Following this recommendation, an unstructured Delaunay triangulation scheme (Fig. 20) was used for all models in the current study.

Figure 21 shows the relative frequency of crack element orientation for the UCS P, S, and Z ($\theta = 45°$) models. A spike in the orientation distribution is associated with the bedding plane orientation, γ, due to crack elements preferably aligned along the DFN cracks. Also, two symmetric peaks can be observed at approximately $\gamma \pm 60°$ due to the adoption throughout the model of a uniform crack element size with triangles tending to an equilateral shape.

The spatial discretization sensitivity of FEM/DEM and, in general, of all DEM models represents a major obstacle in their application to engineering-scale models (e.g.,

simulation of EDZ). For the case of the FEM/DEM-DFN model proposed in this study, the issue is two-fold: (i) element size and (ii) DFN geometry.

As discussed above, a millimetre (or sub-millimetre) element size should be used to correctly capture the mechanical response of the rock material. If such a fine spatial discretization were applied to a model with the size of tens of meters, the total number of triangular and crack elements and associated variables would result in an excessive computational demand. Although increases in computing power have been recently achieved and DEM simulations of entire boundary-values problems attempted (Potyondy and Cundall 2004), the use of this spatial resolution in a large-scale FEM/DEM model is not feasible at the present time. Therefore, further research is needed to reduce the computational requirements of field-scale FEM/DEM simulations by adopting, for example, a continuum-discontinuum approach, whereby only a small-sized region of interest is treated as a FEM/DEM medium whereas the remainder of the domain is modelled as an elastic, non-fracturing medium.

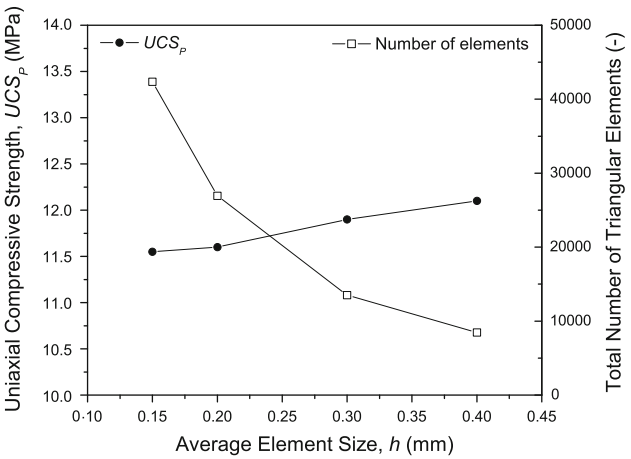

Fig. 19 Element size sensitivity: UCS_P and total number of triangular elements as function of the adopted element size, h

The simulation of strength anisotropy relies upon a closely spaced distribution of short cracks (Table 1). If coarser meshes were to be adopted in the attempt of minimizing the degrees of freedom of the simulation, larger crack spacing and length values will necessarily have to be used. Therefore, the variation of rock representative volume for which the mechanical anisotropy is correctly preserved as the model is up-scaled requires further investigation.

7 Summary and Conclusions

A new modelling approach for anisotropic rocks was developed based on the combined finite-discrete element method (FEM/DEM) (Munjiza 2004). In particular, a transversely isotropic elastic constitutive law was implemented in the Y-Geo FEM/DEM code (Mahabadi et al. 2012a) and a procedure to populate the model with a distribution of preferably oriented fractures was developed. It was shown that the proposed approach is able to capture both the deformation and strength anisotropy that are typical of layered materials.

The said approach was then applied to the laboratory-scale study of the mechanical behavior of Opalinus Clay, an over-consolidated clay shale formation selected to host an underground nuclear waste repository in Switzerland. The model was quantitatively calibrated and validated using experimental values of standard rock mechanics tests.

Following the calibration procedure, a strong agreement between experimentally derived and modeled uniaxial compression test and indirect tension test results was obtained for specimens loaded parallel and perpendicular to layering. Furthermore, a distinctively different crack pattern and failure mechanism was observed for each loading configuration. The simulated stress–strain response exhibited some of the characteristics typically observed in

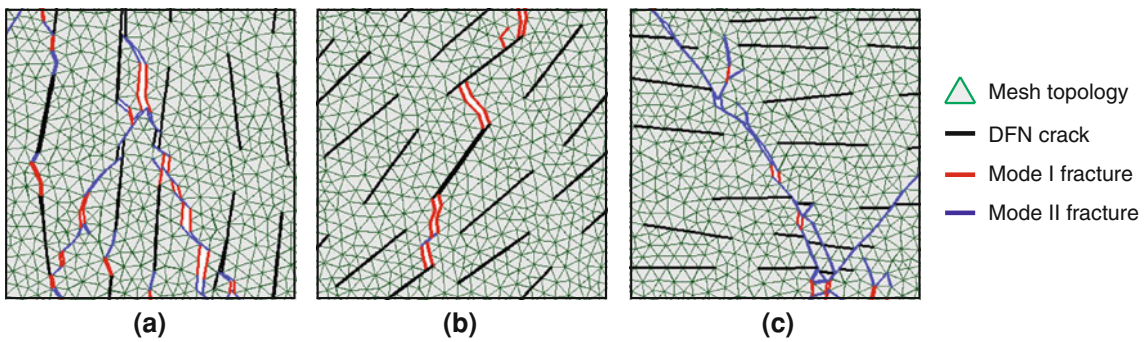

Fig. 20 Zoomed-in views of the center the UCS simulation for the **a** P-sample, **b** Z-sample ($\theta = 45^{o}$), and **c** S-sample, showing the triangular mesh topology, the distribution of pre-existing cracks (DFN) aligned with the bedding plane orientation and several broken crack elements

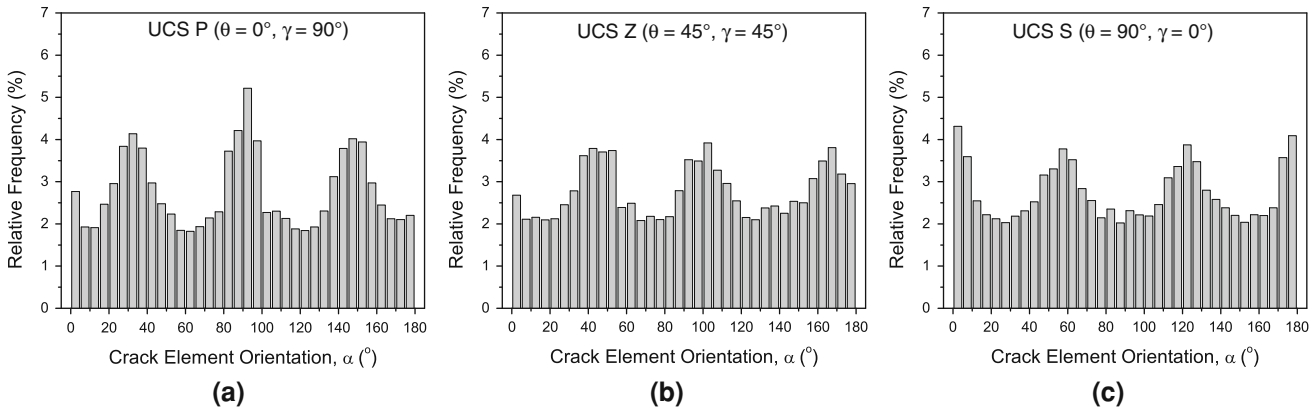

Fig. 21 Relative frequency of crack element orientation for the UCS **a** P-sample, **b** Z-sample ($\theta = 45^{\circ}$), and **c** S-sample

brittle materials, including loss of linearity due to sample damage and post-peak softening.

The effect of confinement on the mechanical behaviour of Opalinus Clay was studied using biaxial compression test models. The simulated failure envelopes corresponded well with the average experimental response of the rock. A characteristic non-linear behaviour was captured for samples loaded in the direction parallel to the bedding at very low confinements due to the transition of the failure mechanism from tensile to shear dominated. A transition from brittle to ductile post-peak behaviour was simulated at a confining pressure of about 7.5 MPa.

A distinctive variation of specimen compressive strength, crack pattern and damage mechanism, was captured as a function of the orientation of specimen anisotropy. These emergent properties of the model were shown to be in good agreement with published experimental findings and were discussed in the context of the theory of brittle failure of rock.

The results presented in this paper represent the first necessary step of a broader-scope project that involves using the FEM/DEM numerical tool to aid in the design of a deep geological repository for nuclear waste in Switzerland. Simulated fracture patterns indicate that the model has the potential to reproduce the EDZ formation mechanisms observed at the Mont Terri URL.

Acknowledgments This work has been supported by the Natural Science and Engineering Research Council of Canada in the form of Discovery Grant No. 341275 and by NAGRA.

References

Adhikary DP, Dyskin AV (1998) A continuum model of layered rock masses with non-associative joint plasticity. Int J Numer Anal Met 22(4):245–261

Amann F, Button EA, Evans KF, Gischig VS, Blümel M (2011) Experimental study of the brittle behaviour of clay shale in rapid unconfined compression. Rock Mech Rock Eng 44(4):415–430

Amann F, Kaiser PK, Button EA (2012) Experimental study of brittle behaviour of clay shale in rapid triaxial compression. Rock Mech Rock Eng 45(1):21–33

Barenblatt GI (1962) The mathematical theory of equilibrium cracks in brittle fracture. Adv Appl Mech 7 (C):55–129

Besuelle P, Chambon R, Collin F (2006) Switching deformation modes in post-localization solutions with a quasi-brittle material. J Mech Mater Struct 1(7):1115–1134

Bieniawski ZT (1967) Mechanism of brittle fracture of rock. Part I: theory of the fracture process. Int J Rock Mech Min Sci 4(4):395–406

Bieniawski ZT, Hawkes I (1978) Suggested methods for determining tensile strength of rock materials. Int J Rock Mech Min Sci 15:99–103

Blümling P, Bernier F, Lebon P, Martin CD (2007) The excavation damaged zone in clay formations time-dependent behaviour and influence on performance assessment. Phys Chem Earth 32(8–14):588–599

Bobet A, Einstein HH (1998a) Fracture coalescence in rock-type materials under uniaxial and biaxial compression. Int J Rock Mech Min Sci 35(7):863–888

Bobet A, Einstein HH (1998b) Numerical modeling of fracture coalescence in a model rock material. Int J Fracture 92(3):221–252

Bock H (2001) RA experiment. Rock mechanics analysis and synthesis: conceptual model of the Opalinus Clay. Mont Terri Technical Note 2001–02

Bock H (2009) RA Experiment. Updated review of the rock mechanics properties of the Opalinus Clay of the Mont Terri URL based on laboratory and field testing. Mont Terri Technical Report 2008–04

Bossart P, Meier PM, Moeri A, Trick T, Mayor J-C (2002) Geological and hydraulic characterisation of the excavation disturbed zone in the Opalinus Clay of the Mont Terri Rock Laboratory. Eng Geol 66(1–2):19–38

Brace WF, Bombolakis EG (1963) A note on brittle crack growth in compression. J Geophys Res 68(12):3709–3713

Brace WF, Paulding BW Jr, Scholz C (1966) Dilatancy in the fracture of crystalline rocks. Geophys Res Lett 71(16):3939–3953

Collin F, Chambon R, Charlier R (2006) A finite element method for poro-mechanical modelling of geotechnical problems using local second gradient models. Int J Numer Meth Eng 65(11):1749–1772

Corkum AG, Martin CD (2007) The mechanical behaviour of weak mudstone (Opalinus Clay) at low stresses. Int J Rock Mech Min Sci 44(2):196–209

Dedecker F, Cundall P, Billaux D, Groeger T (2007) Evaluation of damage-induced permeability using a three-dimensional

adaptive continuum/discontinuum code (AC/DC). Phys Chem Earth 32(8–14):681–690
Diederichs MS (2000) Instability of hard rockmasses: the role of tensile damage and relaxation. PhD Thesis, University of Waterloo, Waterloo, Canada
Diederichs MS (2003) Manuel rocha medal recipient rock fracture and collapse under low confinement conditions. Rock Mech Rock Eng 36(5):339–381
Donath FA (1972) Effects of cohesion and granularity on deformational behavior of anisotropic rock. In: Doc BR, Smith DK (eds) Studies in Mineralogy and Precambrian Geology, vol 135. Geological Society of America, USA, pp 95–128
Dugdale DS (1960) Yielding of steel sheets containing slits. J Mech Phys Solids 8(2):100–104
Duveau G, Shao JF, Henry JP (1998) Assessment of some failure criteria for strongly anisotropic geomaterials. Mech Cohes-Frict Mat 3(1):1–26
Evans R, Marathe M (1968) Microcracking and stress-strain curves for concrete in tension. Mater Struct 1(1):61–64
Hillerborg A, Modeer M, Petersson P-E (1976) Analysis of crack formation and crack growth in concrete by means of fracture mechanics and finite elements. Cement Concrete Res 6(6):773–781
Hoek E, Brown ET (1980) Strength of jointed rock masses. Geotechnique 33(3):187–223
Horii H, Nemat-Nasser S (1986) Brittle failure in compression: splitting, faulting, and brittle-ductile transition. Philos T R Soc Lond 319:337–374
Itasca Consulting Group Inc (2012) FLAC. Fast Lagrangian Analysis of Continua, Version 7.0. Minneapolis, USA
Jaeger JC, Cook NGW (1976) Fundamentals of rock mechanics. Chapman & Hall, London
Jahns (2010) RA Experiment. Opalinus Clay rock characterization. Mont Terri Technical Note 2008–55rev
Jia P, Tang CA (2008) Numerical study on failure mechanism of tunnel in jointed rock mass. Tunn Undergr Sp Tech 23(5):500–507
Kaiser PK, Kim BH (2008) Rock mechanics advances of underground constructions and mining. In: Proceedings of the Korean rock mechanics symposium. Seoul, Korea, pp 1–6
Kemeny J, Cook NGW (1986) Effective moduli, non-linear deformation and strength of a cracked elastic solid. Int J Rock Mech Min Sci 23(2):107–118
Klinkenberg M, Kaufhold S, Dohrmann R, Siegesmund S (2009) Influence of carbonate microfabrics on the failure strength of claystones. Eng Geol 107(1–2):42–54
Konietzky H, Blümling P, teKamp L (2003) Opalinuston—Felsmechanische Untersuchungen. Interner Bericht 03-08, NAGRA, Wettingen, Switzerland
Labiouse V (2012) Hollow cylinder simulation experiments on Boom, Opalinus, Callovo-Oxfordian Clays. International Post-TIMODAZ Workshop, St-Ursanne, Switzerland, 6–7 February 2012
Labuz JF, Shah SP, Dowding CH (1985) Experimental analysis of crack propagation in granite. Int J Rock Mech Min Sci 22(2):85–98
Lan H, Martin CD, Hu B (2010) Effect of heterogeneity of brittle rock on micro-mechanical extensile behaviour during compression loading. J Geophys Res 115:1–14
Mahabadi OK (2012) Investigating the influence of micro-scale heterogeneity and microstructure on the failure and mechanical behaviour of geomaterials. PhD thesis, University of Toronto, Toronto, Canada
Mahabadi OK, Grasselli G, Munjiza A (2010) Y-GUI: A graphical user interface and pre-processor for the combined finite-discrete element code, Y2D, incorporating material inhomogeneity. Comput Geosci 36(2):241–252
Mahabadi OK, Lisjak A, Grasselli G, Munjiza A (2012a) Y-Geo: a new combined finite-discrete element numerical code for geomechanical applications. Int J Geomech. doi:10.1061/(ASCE)GM.1943-5622.0000216
Mahabadi OK, Randall NX, Zong Z, Grasselli G (2012b) A novel approach for micro-mechanical characterization and modelling of geomaterials incorporating actual material heterogeneity. Geophys Res Lett 39:L01303
Martin CD (1997) Seventeenth Canadian geotechnical colloquium: the effect of cohesion loss and stress path on brittle rock strength. Can Geotech J 34:239–254
McLamore R, Gray KE (1967) The mechanical behavior of anisotropic sedimentary rocks. J Eng Ind-T Asme 89:62–73
Munjiza A (2004) The combined finite-discrete element method. Wiley, Chichester
Munjiza A, Andrews KRF (2000) Discretised penalty function method in combined finite-discrete element analysis. Int J Num Meth Eng 49(11):1495–1520
Munjiza A, John NWM (2002) Mesh size sensitivity of the combined FEM/DEM fracture and fragmentation algorithms. Eng Fract Mech 69(2):281–295
Munjiza A, Owen DRJ, Bicanic N (1995) A combined finite-discrete element method in transient dynamics of fracturing solids. Eng Computation 12(2):145–174
Munjiza A, Andrews KRF, White JK (1999) Combined single and smeared crack model in combined finite-discrete element analysis. Int J Num Meth Eng 44(1):41–57
Naumann M, Hunsche U, Schulze O (2007) Experimental investigations on anisotropy in dilatancy, failure and creep of Opalinus Clay. Phys Chem Earth 32(8–14):889–895
Niandou H, Shao JF, Henry JP, Fourmaintraux D (1997) Laboratory investigation of the mechanical behavior of Tournemire shale. Int J Rock Mech Min Sci 34(1):3–16
Paterson MS, Wong T (2004) Experimental Rock Deformation—The Brittle Field. Springer, NewYork
Popp T, Salzer K (2007a) Anisotropy of seismic and mechanical properties of Opalinus Clay during triaxial deformation in a multi-anvil apparatus. Phys Chem Earth 32(8–14):879–888
Popp T, Salzer K (2007b) Laboratory tests on bedding planes. Mont Terri Technical Report 2007–04
Popp T, Salzer K, Minkley W (2008) Influence of bedding planes to EDZ-evolution and the coupled HM properties of Opalinus Clay. Phys Chem Earth 33:S374–S387
Potyondy D, Cundall P (2000) Bonded-particle simulations of the in situ failure test at Olkiluoto. International Progress Report 01–13, SKB, Stockholm, Sweden
Potyondy DO, Cundall PA (2004) A bonded-particle model for rock. Int J Rock Mech Min Sci 41(8):1329–1364
Riahi A, Curran JH (2009) Full 3D finite element Cosserat formulation with application in layered structures. Appl Math Model 33(8):3450–3464
Salager S, Nuth M, Laloui L (2010) Anisotropic features of the mechanical behaviour of Opalinus Clay. In: Zhao J, Labiouse V, Dudt J-P, Mathier J-F (eds) Proceedings of the European Rock Mechanics Symposium, Lausanne, Switzerland. Taylor & Francis Group, London
Seeska R, Lux K-H (2012) Borehole deformation measurements and video-observations of boreholes in the Opalinus Clay of the Mont Terri URL. International Post-TIMODAZ Workshop, St-Ursanne, Switzerland, 6–7 February 2012
Tang CA, Kaiser PK (1998) Numerical simulation of cumulative damage and seismic energy release during brittle rock failure - Part I: fundamentals. Int J Rock Mech Min Sci 35(2):113–121
Tang CA, Kou SQ (1998) Crack propagation and coalescence in brittle materials under compression. Eng Fract Mech 61(3–4):311–324
Tang CA, Lin P, Wong RHC, Chau KT (2001) Analysis of crack coalescence in rock-like materials containing three flaws—Part II: numerical approach. Int J Rock Mech Min Sci 38(7):925–939

Tapponnier P, Brace WF (1976) Development of stress-induced microcracks in Westerly Granite. Int J Rock Mech Min Sci 13(4): 103–112

Tijssens MGA, Sluys BLG, van der Giessen E (2000) Numerical simulation of quasi-brittle fracture using damaging cohesive surfaces. Eur J Mech A-Solid 19(5):761–779

Ting TCT (1996) Anisotropic elasticity: theory and applications. Oxford University Press

Tsang C-F, Bernier F, Davies C (2005) Geohydromechanical processes in the excavation damaged zone in crystalline rock, rock salt, and indurated and plastic clays—in the context of radioactive waste disposal. Int J Rock Mech Min Sci 42(1):109–125

Turon A, Dávila CG, Camanho PP, Costa J (2007) An engineering solution to mesh size effects in the simulation of delamination using cohesive zone models. Eng Fract Mech 74(10):1665–1682

Vesga LF, Vallejo LE, Lobo-Guerrero S (2008) DEM analysis of the crack propagation in brittle clays under uniaxial compression tests. Int J Num Anal Meth 32(11):1405–1415

Vietor T, Li X, Fierz T (2012) In situ experiments in TIMODAZ. International Post-TIMODAZ Workshop, St-Ursanne, Switzerland, 6–7 February 2012

Wanne T (2002) Rock strength and deformation dependence on schistosity. Simulation of rock with PFC3D. Report 2002–05, Posiva Oy, Helsinki, Finland

Yan M (2008) Numerical modelling of brittle fracture and step-path failure: from laboratory to rock slope scale. PhD Thesis, Simon Fraser University, Burnaby, Canada

You S, Zhao G, Ji H (2011) Model for transversely isotropic materials based on distinct lattice spring model (DLSM). J Computer 6:1139–1144